IJCRT.ORG ISSN : 2320-2882

INTERNATIONAL JOURNAL OF CREATIVE RESEARCH THOUGHTS (IJCRT)

An International Open Access, Peer-reviewed, Refereed Journal

CHANDRAYAAN-2 DFSAR POLARIMETRIC MAPPING OF CANDIDATE VOLATILE-RETENTION ENVIRONMENTS IN THE LUNAR SOUTH POLAR REGION

[1]Vivek Kumar Dabhole, [2]Dr. Sayyad Shafiyoddin Badruddin
[1]Research Scholar in Electronics Science, [2]Professor of Physics and Research Guide
[1,2]Milliya Arts, Science and Management Science College, Beed, Maharashtra, India-431122
Affiliated to Dr Babasaheb Ambedkar Marathwada University, Chhatrapati Sambhajinagar, India

Abstract: This study investigates candidate volatile-retention environments in the lunar south polar region using a Chandrayaan-2 Dual-Frequency Synthetic Aperture Radar (DFSAR) fully polarimetric L-band scene acquired during Orbit 879. The 05 November 2019 Stripmap dataset contains HH, HV, VH, and VV channels and covers terrain centred near 85.822265°S, 114.701166°E. A T3 coherency-matrix workflow was used to derive Pauli RGB, H/A/Alpha parameters, Entropy-Alpha and Entropy-Theta distributions, eigenvalue structure, Yamaguchi four-component and model-free decompositions, Circular Polarisation Ratio (CPR), Degree of Polarisation (DoP), and a combined CPR-DoP candidate mask. The mean entropy, anisotropy, and alpha angle are 0.536, 0.362, and 24.27°, respectively, while the normalised eigenvalues are 0.797, 0.137, and 0.064. Surface scattering dominates the backscatter power (65.25%), followed by a substantial volume component (32.36%); double-bounce and helix contributions are 0.08% and 2.31%. The candidate classification identifies 303,166 pixels, corresponding to 7.6040% of 3,986,944 analysed pixels. These pixels form 103,878 predominantly small clusters with a mean size of 2.92 pixels and a maximum size of 75 pixels. The results indicate a mature, surface-controlled regolith containing localised porous or fractured zones that enhance depolarisation and volume scattering. Such zones are interpreted as candidate environments for retaining hydrogen-bearing species; however, the radar signatures are not treated as direct proof of water ice.

Index Terms - Chandrayaan-2 DFSAR, lunar south pole, polarimetric SAR, CPR, degree of polarisation, volatile retention, water-ice candidates.

I. INTRODUCTION

The lunar polar regions are central to current planetary exploration because permanently shadowed and thermally stable environments can preserve hydrogen-bearing species over geological timescales. Neutron spectroscopy, thermal measurements, imaging spectroscopy, and radar observations have independently indicated polar hydrogen enrichment, cold-trapping conditions, and locally exposed water ice [2]-[5]. Radar is especially valuable in high-latitude terrain because it operates independently of solar illumination and can respond to roughness, blockiness, dielectric contrasts, and multiple scattering within the upper regolith.

The interpretation of lunar radar anomalies nevertheless remains non-unique. Elevated circular polarisation ratio (CPR) may result from coherent backscatter or volume scattering in ice-bearing material. Still, it can also be produced by rough crater walls, blocky ejecta, or unfavourable local incidence geometry [6], [7]. Consequently, CPR should be evaluated together with complementary parameters that describe depolarisation, entropy, eigenstructure, and the relative contributions of surface, volume, and double-bounce scattering. Full-polarimetric observations are well suited to this task because they retain the complete scattering matrix and permit physically interpretable target decompositions.

The Chandrayaan-2 DFSAR instrument provides L- and S-band observations with multiple polarimetric modes and is the first lunar radar to acquire fully polarimetric L-band data [1]. The longer L-band wavelength offers enhanced sensitivity to the upper regolith and shallow subsurface compared with shorter-wavelength systems. This paper condenses the Orbit 879 analysis into an integrated research framework. The objectives are to: (i) characterise the dominant scattering regime using H/A/Alpha and eigenvalue analyses; (ii) quantify surface, volume, double-bounce, and helix contributions; (iii) evaluate CPR and DoP patterns; and (iv) map and statistically characterise candidate volatile-retention environments.

II. STUDY AREA AND DATASET

The analysed dataset, ch2_sar_ncxl_20191105t061840380_d_fp_d18, was acquired on 05 November 2019 during Chandrayaan-2 Orbit 879 in ascending Stripmap mode. It is a fully polarimetric L-band product containing HH, HV, VH, and VV channels. The look angle is approximately 26.0°, the spacecraft altitude is 88.172 km, and the processed scene contains 4676 × 5581 pixels across a 10.475 km swath.

The scene lies within the lunar south polar region and is centred at 85.822265°S and 114.701166°E. Its geographic extent is approximately 82.998°S-88.050°S and 73.515°E-155.203°E, covering terrain in the broader Amundsen crater sector and adjacent highlands. This high-latitude setting includes very cold and potentially shadowed environments that are relevant to volatile preservation. The elongated footprint and wide longitudinal coverage also provide a useful test case for evaluating spatial variability in scattering and candidate-pixel density.

III. METHODOLOGY

A. Polarimetric parameter generation

The full-polarimetric channels were represented through the 3 × 3 T3 coherency matrix. The eigenvalue-eigenvector framework of Cloude and Pottier [8] was used to derive entropy (H), anisotropy (A), alpha angle (α), and normalised eigenvalues e1, e2, and e3. Entropy measures scattering randomness, anisotropy describes the relative importance of secondary mechanisms, and alpha angle indicates the dominant scattering type. The parameters were evaluated individually and through the H-α, three-dimensional H-A-α, and H-θ distributions.

Pauli RGB imagery was used for qualitative visualisation of surface, volume, and double-bounce responses. Scattering power was quantified using the Yamaguchi four-component decomposition [9], which separates surface (Ps), double-bounce (Pd), volume (Pv), and helix (Ph) components. A model-free three-component decomposition was also examined as an independent check on the relative dominance of surface, volume, and double-bounce scattering.

B. CPR, DoP, and candidate classification

CPR was derived as an indicator of same-sense versus opposite-sense circularly polarised backscatter and therefore of multiple-scattering behaviour. DoP was used as a complementary measure of the fraction of the returned signal remaining polarised. Low DoP represents stronger depolarisation and is commonly associated with heterogeneous, rough, porous, or internally scattering media. The candidate mask was produced by the simultaneous CPR-DoP criterion adopted in the processing workflow: pixels meeting the prescribed pair of conditions were assigned a candidate value of one, while all other pixels were assigned zero. Because roughness can mimic ice-related radar signatures, the resulting mask is interpreted as candidate volatile-retention terrain rather than confirmed ice.

C. Spatial and cluster statistics

The binary candidate map was used to calculate the total number and percentage of candidate pixels. Connected candidate pixels were grouped into clusters, from which the number of clusters, mean cluster size, and maximum cluster size were obtained. To evaluate along-track variability, the scene was divided into horizontal stripes and candidate density was computed for each stripe. These statistics distinguish extensive continuous deposits from small, localised micro-environments distributed through a predominantly non-candidate regolith.

IV. RESULTS

A. H/A/Alpha and eigenvalue structure

The mean entropy is 0.536, with a range of 0.000-0.994, indicating a moderately heterogeneous scattering environment. The mean anisotropy is 0.362 (range 0.000-0.899), demonstrating measurable but subordinate secondary mechanisms. The mean alpha angle is 24.27° (range 0.00°-81.27°), placing the dominant response in the surface or odd-bounce regime. Most H-α observations occupy the H5-H7 zones and form an elongated distribution from low-entropy/low-alpha toward moderate-to-high entropy and alpha. This pattern represents a surface-controlled regolith with local transitions toward more complex volume-scattering behaviour.

The normalised eigenvalues are e1 = 0.797, e2 = 0.137, and e3 = 0.064. The primary eigenvalue therefore accounts for approximately 79.7% of the eigenvalue sum, while the combined secondary contribution is 20.1%. This confirms that one mechanism dominates most pixels but also shows that local structural heterogeneity is not negligible. The three-dimensional H-A-α distribution is densest at moderate entropy and anisotropy and at alpha angles below approximately 40°, consistent with gradual rather than abrupt changes in regolith properties.

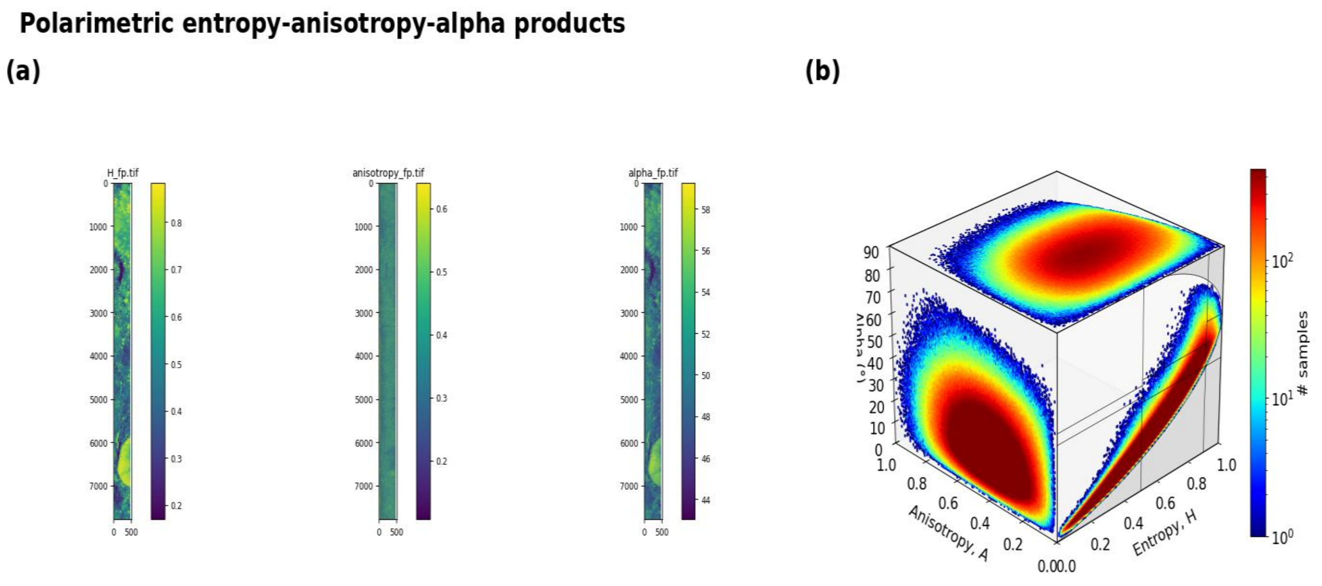

Fig. 1. Polarimetric products derived from the T3 coherency matrix: (a) entropy, anisotropy, and alpha-angle maps;
(b) three-dimensional H-A-α density distribution.

B. Scattering decomposition and orientation behaviour

The Yamaguchi decomposition assigns 65.25% of total backscatter power to surface scattering, 32.36% to volume scattering, 0.08% to double-bounce scattering, and 2.31% to helix scattering. Surface scattering is thus about twice the volume contribution and clearly controls the scene-average response. The negligible double-bounce term indicates that steep dihedral-like geometries occupy only a very small fraction of the footprint. The model-free decomposition gives the same first-order interpretation, supporting the robustness of the surface-dominated result.

The 32.36% volume component is nevertheless substantial and is concentrated in localised zones. In lunar regolith, enhanced volume scattering can be produced by porosity, impact-fractured deposits, buried ejecta, grain-size variability, and rough shallow-subsurface layers. The H-θ distribution forms a crescent-shaped cluster concentrated mainly at moderate entropy and positive orientation values. Its limited occupancy of strongly oriented regions agrees with the very small double-bounce component. It suggests that internal heterogeneity, rather than large organised structures, is the principal source of scattering complexity.

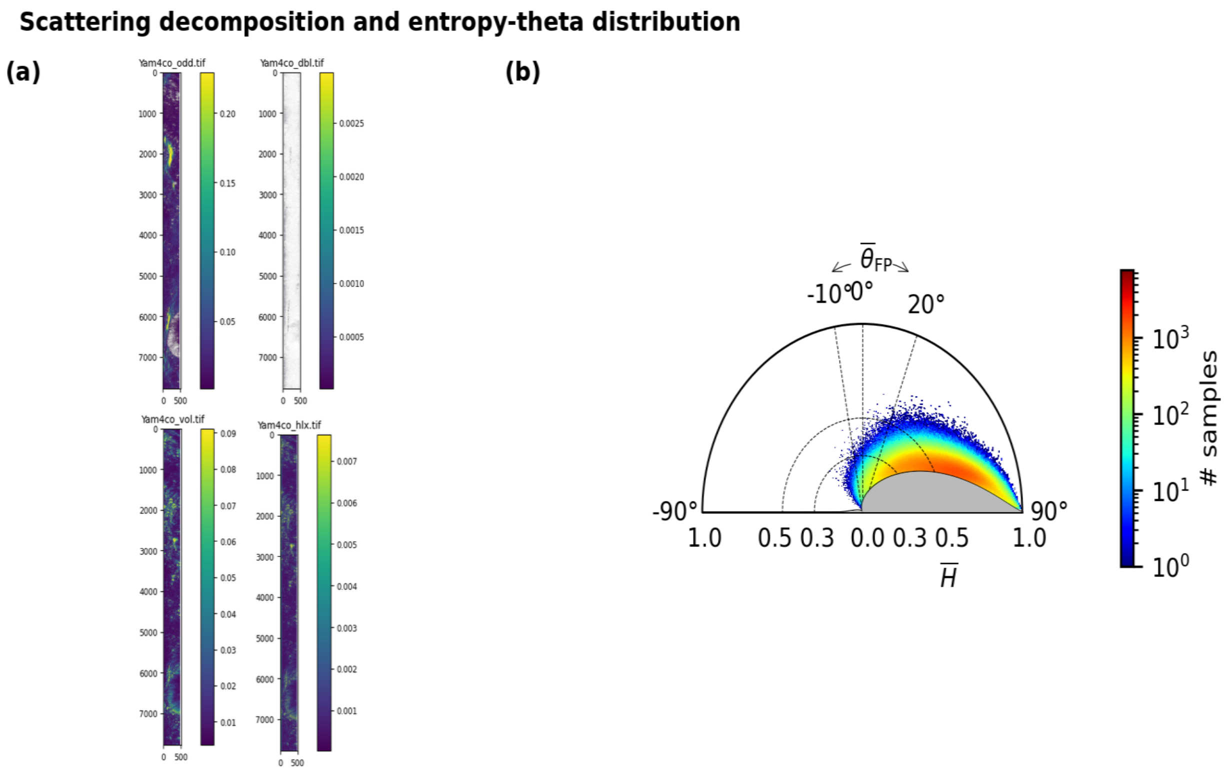

Fig. 2. (a) Yamaguchi four-component scattering-power maps and (b) Entropy-Theta density distribution for Orbit 879.

Table 1. Integrated polarimetric indicators for the Orbit 879 scene

Parameter	Result	Interpretation
Entropy (H)	0.536; range 0.000-0.994	Moderate scattering randomness and heterogeneity
Anisotropy (A)	0.362; range 0.000-0.899	Secondary mechanisms are measurable but subordinate
Alpha angle (α)	24.27°; range 0.00°-81.27°	Dominantly surface/odd-bounce scattering
Normalised eigenvalues	e1=0.797, e2=0.137, e3=0.064	Strong primary mechanism with local secondary scattering
Surface scattering	65.25%	Upper regolith controls most backscatter
Volume scattering	32.36%	Substantial local internal heterogeneity
Double-bounce / helix	0.08% / 2.31%	Very limited dihedral and asymmetric scattering

C. CPR, DoP, and candidate distribution

The CPR map is comparatively uniform, with most pixels visually concentrated near approximately 1.0-1.2. The absence of extensive very high CPR zones indicates that large-scale strong multiple-scattering anomalies are not widespread. This uniformity is consistent with a mature surface-controlled terrain, while modest local CPR variations are compatible with the observed volume-scattering component. CPR alone therefore does not isolate a unique ice-related response.

The DoP map exhibits much stronger spatial variation. Most of the footprint retains moderate-to-high polarisation, but local low-DoP zones indicate enhanced depolarisation and internal scattering. The most prominent low-DoP features occur in portions of the lower scene and spatially coincide with regions of increased entropy and structural complexity. The combined CPR-DoP mask produces a fragmented pattern of candidate pixels rather than a continuous deposit, demonstrating that the favourable scattering combination is restricted to localised parts of the regolith.

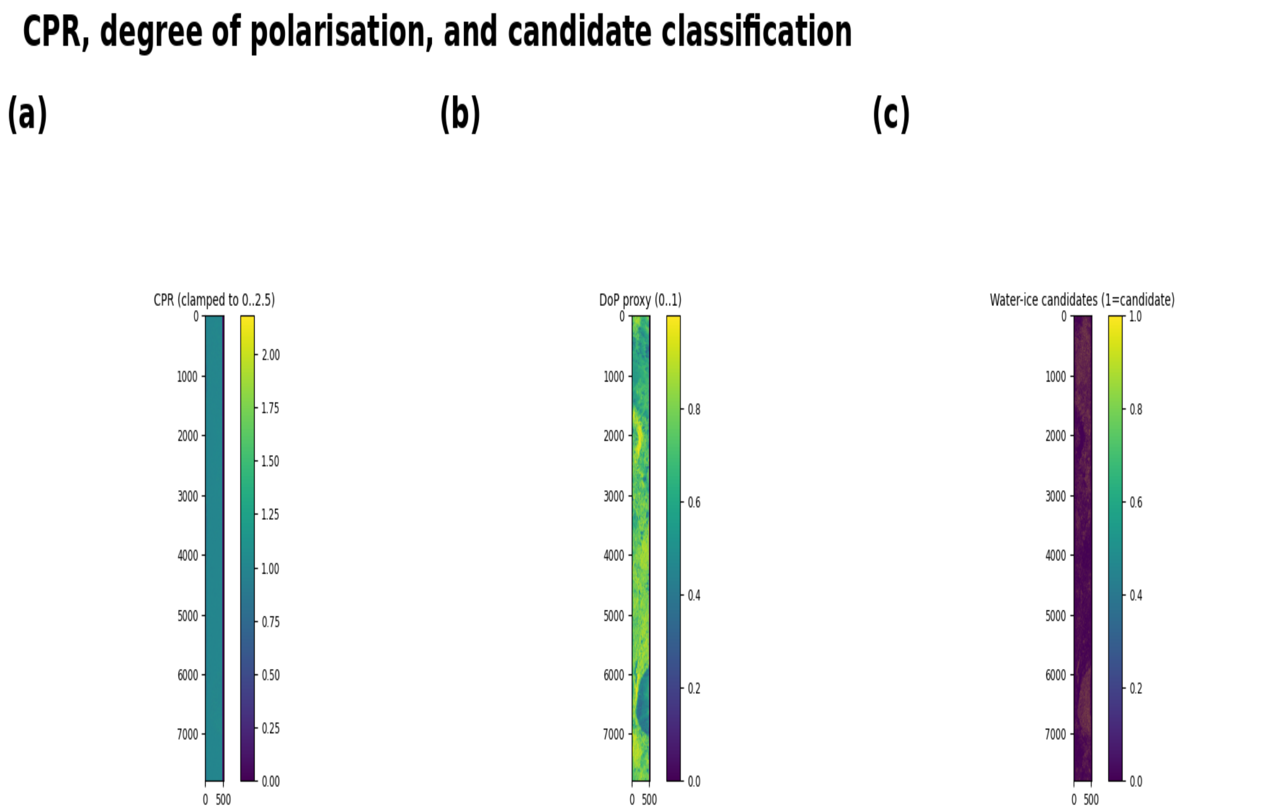

Fig. 3. (a) Circular Polarisation Ratio, (b) Degree of Polarisation, and (c) binary candidate volatile-retention map derived from their combined interpretation.

D. Candidate abundance, clusters, and density variability

Of the 3,986,944 analysed pixels, 303,166 are classified as candidates and 3,683,778 as non-candidates. The candidate fraction is therefore 7.6040%, whereas non-candidate terrain accounts for 92.3960%. Candidate pixels occur in 103,878 clusters. The mean cluster size is only 2.92 pixels, and the maximum reported cluster size is 75 pixels, showing that most occurrences are small and isolated. These statistics do not support a scene-wide continuous deposit; instead, they describe numerous micro-environments embedded in a predominantly surface-dominated regolith.

Stripe-wise candidate density varies from less than 3% in the sparsest portion to more than 14% in the densest portion. The overall stripe-index relationship is moderately negative ($r = -0.4663$), although the profile is non-monotonic and contains a secondary high-density interval. The variability indicates that candidate occurrence is governed by local changes in roughness, porosity, fracture density, impact history, and shallow-subsurface structure rather than by a uniform regional process.

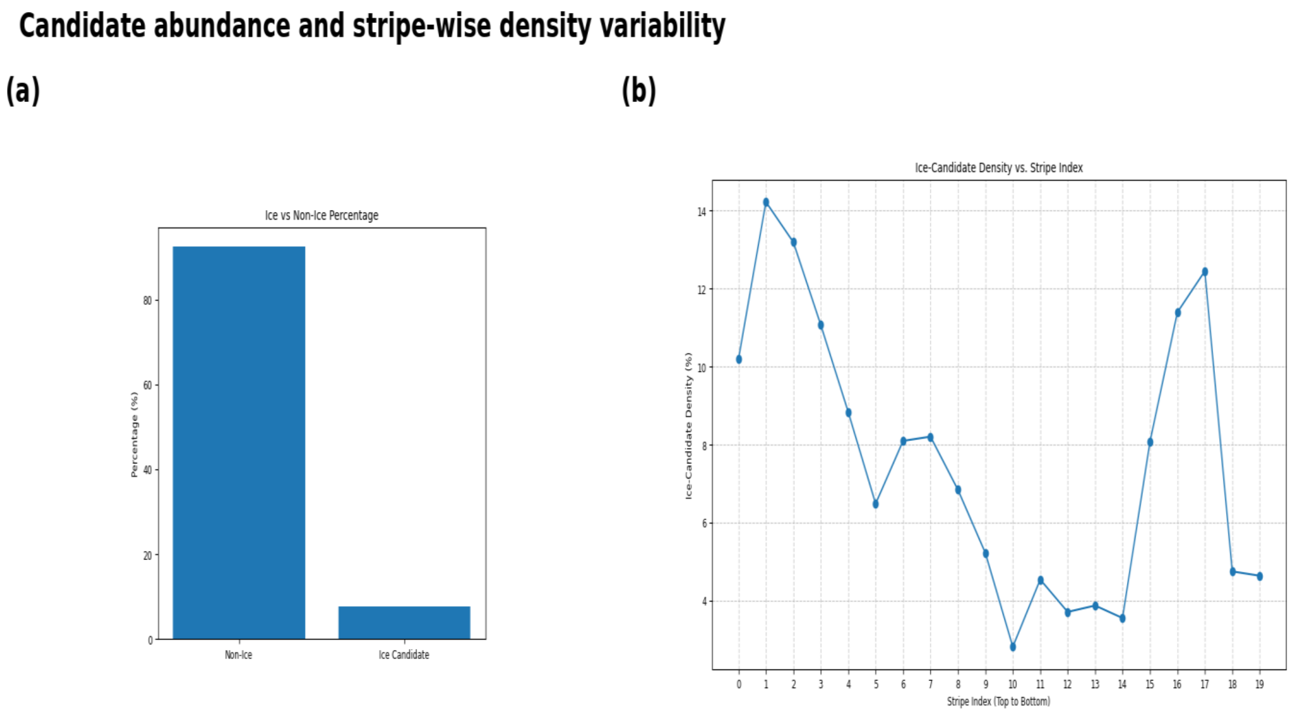

Fig. 4. (a) Percentage of candidate and non-candidate terrain and (b) stripe-wise candidate density from the top to the bottom of the scene.

Table 2. Candidate classification and cluster statistics

Metric	Value
Total analysed pixels	3,986,944
Candidate pixels	303,166
Non-candidate pixels	3,683,778
Candidate/non-candidate terrain	7.6040% / 92.3960%
Number of candidate clusters	103,878
Mean cluster size	2.92 pixels
Maximum cluster size	75 pixels
Stripe-index correlation	r = -0.4663

V. DISCUSSION

The integrated result is a mature, predominantly surface-controlled lunar regolith containing localised zones of higher structural complexity. The low mean alpha angle, dominant first eigenvalue, and 65.25% surface component all show that most radar energy interacts with the upper regolith through a principal surface-scattering mechanism. At the same time, moderate entropy, measurable secondary eigenvalues, and 32.36% volume scattering demonstrate that the scene is not homogeneous. Impact gardening, ejecta emplacement, micrometeorite bombardment, thermal cycling, and long-term space weathering can create the pores, fractures, and grain-scale contrasts responsible for these local volume-scattering zones.

The candidate map links the polarimetric observations to a process-based interpretation of hydrogen retention. Solar-wind protons may be implanted widely, but efficient retention should be favoured where the regolith contains protected pore spaces and internal scattering pathways. The candidate pixels occur where the radar response simultaneously indicates multiple scattering and depolarisation, and their fragmented cluster geometry is consistent with unevenly distributed structural modification. The small mean cluster size is therefore physically meaningful: it suggests that favourable retention conditions develop as local micro-environments rather than as a uniformly ice-rich layer.

A conceptual sequence supported by the results is: solar-wind irradiation → hydrogen implantation → regolith evolution and structural modification → porosity and fracture development → enhanced volume scattering and depolarisation → localised hydrogen retention → candidate volatile-retention environments. This sequence does not imply that every candidate pixel contains water ice. Radar ambiguity remains fundamental because rough and blocky materials can also produce elevated CPR or reduced polarisation [6], [7], and recent full-polarimetric lunar studies continue to emphasise the need to separate compositional effects from surface morphology [10].

VI. LIMITATIONS AND FUTURE WORK

The analysis is based on a single L-band scene and therefore represents the physical conditions of Orbit 879 rather than the entire lunar south polar region. The candidate classification depends on the adopted CPR-DoP thresholds, and the source chapter does not provide an independent compositional validation for each candidate pixel. In addition, local incidence-angle effects, slopes, crater-wall roughness, and residual processing artefacts can influence the radar parameters. These limitations require the mapped pixels to be described as candidates rather than confirmed ice deposits.

Future work should co-register the candidate map with Diviner temperature, LOLA topography and slope, LROC imagery, neutron-derived hydrogen abundance, and near-infrared OH/H2O products. Multi-incidence and dual-frequency comparisons would help distinguish roughness-driven CPR enhancement from genuine volume scattering. Repeating the same integrated workflow over additional south- and north-polar DFSAR scenes would also test whether the Orbit 879 candidate fraction and cluster geometry are representative or locally anomalous.

VII. CONCLUSION

Chandrayaan-2 DFSAR fully polarimetric L-band data provide a detailed view of scattering and candidate volatile-retention environments in the lunar south polar region. Orbit 879 is dominated by surface scattering (65.25%) but contains a substantial volume component (32.36%), moderate entropy (0.536), moderate anisotropy (0.362), and a low mean alpha angle (24.27°). The eigenvalue structure confirms a dominant primary mechanism with measurable secondary scattering.

The integrated CPR-DoP classification identifies 303,166 candidate pixels, or 7.6040% of the analysed scene. Their organisation into 103,878 small clusters demonstrates that favourable scattering environments are highly fragmented and localised. The results support an interpretation in which porous, fractured, and structurally heterogeneous regolith retains hydrogen-bearing species more effectively than compact surface-dominated terrain. The mapped signatures are therefore useful for prioritising candidate volatile-retention zones, while confirmation of water ice requires independent thermal, topographic, spectral, and compositional evidence.

ACKNOWLEDGMENT

The authors acknowledge the Indian Space Research Organisation (ISRO) and the Indian Space Science Data Centre for the Chandrayaan-2 DFSAR data used in this study.

REFERENCES

[1] S. S. Bhiravarasu et al., “Chandrayaan-2 Dual-Frequency SAR (DFSAR): Performance Characterisation and Initial Results,” The Planetary Science Journal, vol. 2, no. 4, art. 134, 2021, doi: 10.3847/PSJ/abfdbf.

[2] S. Li et al., “Direct evidence of surface exposed water ice in the lunar polar regions,” Proceedings of the National Academy of Sciences, vol. 115, no. 36, pp. 8907-8912, 2018, doi: 10.1073/pnas.1802345115.

[3] D. A. Paige et al., “Diviner Lunar Radiometer observations of cold traps in the Moon’s south polar region,” Science, vol. 330, no. 6003, pp. 479-482, 2010, doi: 10.1126/science.1187726.

[4] W. C. Feldman et al., “Fluxes of fast and epithermal neutrons from Lunar Prospector: Evidence for water ice at the lunar poles,” Science, vol. 281, no. 5382, pp. 1496-1500, 1998, doi: 10.1126/science.281.5382.1496.

[5] P. D. Spudis et al., "Evidence for water ice on the Moon: Results for anomalous polar craters from the LRO Mini-RF imaging radar," Journal of Geophysical Research: Planets, vol. 118, no. 10, pp. 2016-2029, 2013, doi: 10.1002/jgre.20156.

[6] W. Fa and Y. Cai, "Circular polarisation ratio characteristics of impact craters from Mini-RF observations and implications for ice detection at the polar regions of the Moon," Journal of Geophysical Research: Planets, vol. 118, no. 8, pp. 1582-1608, 2013, doi: 10.1002/jgre.20110.

[7] B. J. Thomson et al., "An upper limit for ice in Shackleton crater as revealed by LRO Mini-RF orbital radar," Geophysical Research Letters, vol. 39, art. L14201, 2012, doi: 10.1029/2012GL052119.

[8] S. R. Cloude and E. Pottier, "An entropy-based classification scheme for land applications of polarimetric SAR," IEEE Transactions on Geoscience and Remote Sensing, vol. 35, no. 1, pp. 68-78, 1997, doi: 10.1109/36.551935.

[9] Y. Yamaguchi, T. Moriyama, M. Ishido, and H. Yamada, "Four-component scattering model for polarimetric SAR image decomposition," IEEE Transactions on Geoscience and Remote Sensing, vol. 43, no. 8, pp. 1699-1706, 2005, doi: 10.1109/TGRS.2005.852084.

[10] D. Putrevu et al., "Lunar impact craters: New perspectives from full-polarimetric analysis of Chandrayaan-2 dual-frequency SAR data," Journal of Geophysical Research: Planets, vol. 128, no. 12, e2023JE007745, 2023, doi: 10.1029/2023JE007745.